

**This is an electronic reprint of the original article.  
This reprint *may differ* from the original in pagination and typographic detail.**

**Author(s):** Bazhenov, Andrey; Kauppinen, Minttu; Honkala, Karoliina

**Title:** DFT Prediction of Enhanced Reducibility of Monoclinic Zirconia upon Rhodium Deposition

**Year:** 2018

**Version:**

**Please cite the original version:**

Bazhenov, A., Kauppinen, M., & Honkala, K. (2018). DFT Prediction of Enhanced Reducibility of Monoclinic Zirconia upon Rhodium Deposition. *Journal of Physical Chemistry C*, 122(12), 6774-6778. <https://doi.org/10.1021/acs.jpcc.8b01046>

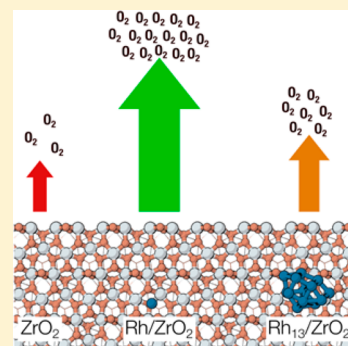
All material supplied via JYX is protected by copyright and other intellectual property rights, and duplication or sale of all or part of any of the repository collections is not permitted, except that material may be duplicated by you for your research use or educational purposes in electronic or print form. You must obtain permission for any other use. Electronic or print copies may not be offered, whether for sale or otherwise to anyone who is not an authorised user.

# DFT Prediction of Enhanced Reducibility of Monoclinic Zirconia upon Rhodium Deposition

Andrey S. Bazhenov, Minttu M. Kauppinen, and Karoliina Honkala\*

Department of Chemistry, Nanoscience Center, University of Jyväskylä, P.O. Box 35, FI-40014 Jyväskylä, Finland

**ABSTRACT:** Oxides are an important class of materials and are widely used, for example, as supports in heterogeneous catalysis. In a number of industrial catalytic processes, oxide supports actively participate in chemical transformations by releasing lattice oxygen anions. While this is intuitively understood for reducible oxides, the reducibility of irreducible oxides may be modified via nanoengineering or upon inclusion of foreign species. Our calculations predict that the ability of irreducible monoclinic zirconia to release oxygen improves substantially upon deposition of rhodium. Through a comprehensive screening of Rh/ZrO<sub>2</sub> with different size of the rhodium species, we find that a Rh adatom and a Rh<sub>4</sub> nanocluster have the largest impact on the reducibility of zirconia. With increasing size the effect of rhodium decays. Our findings demonstrate that the phenomenon of enhanced reducibility of irreducible oxides in the presence of metals should be considered when interpreting experimental and computational results, as reactions that involve release of oxygen from an oxide support might be possible for irreducible oxides.



## INTRODUCTION

Oxide materials are found in a variety of industrial applications ranging from electronics to heterogeneous catalysis,<sup>1–3</sup> where they are widely used as supporting materials or active catalytic components. Among the industrially important processes, the water–gas shift (WGS) reaction is pivotal for obtaining chemicals and fuels.<sup>4,5</sup> However, the precise reaction mechanism of the WGS reaction has remained a controversial issue, partly due to the undefined role of the support. A series of computational and experimental studies has demonstrated that the WGS reaction proceeds via the so-called “redox” route,<sup>6–8</sup> where the abstraction of oxygen from the oxide is one of the reaction steps. While the “redox” mechanism is obvious in catalytic systems based on reducible oxides, it has also been suggested to be viable for their irreducible counterparts.<sup>8,9</sup>

A number of reports indicates that the reducibility of oxides may be tailored. Growth of thin films, nanoshaping, and doping have been shown to improve the oxygen release from oxides. Furthermore, it has been suggested that formation of metal/oxide interfaces upon deposition of metal species might also impact on the reducibility. These approaches have been extensively studied for reducible oxides.<sup>10–14</sup> However, less attention has been paid to irreducible oxides, such as ZrO<sub>2</sub>, a prominent catalyst component in the WGS reaction. Several experimental studies have suggested that the release of oxygen is facilitated by the presence of metals in ZrO<sub>2</sub>-based catalytic materials.<sup>6,7,15–18</sup> These catalysts are predominantly composed of monoclinic zirconia, which is typically the most active phase of zirconia for the WGS reaction.<sup>8,9,19–21</sup> Recent computational studies predict the reduction of vacancy formation energy for some metal/irreducible oxide combinations. The decrease is mild for, for example, MgO,<sup>22</sup> and is up to 60% for Au on a highly symmetrical tetragonal ZrO<sub>2</sub> (101) surface.<sup>23,24</sup> Interestingly, the identity of the metal seems to have an impact on the

vacancy formation energy on tetragonal zirconia<sup>23,24</sup> based on results for a Ru<sub>10</sub> cluster and Au metal nanostructures containing at most 10 atoms. However, it is yet to be determined how metal-enhanced reducibility of zirconia evolves for even larger nanostructures than studied so far.

Herein we report computational predictions of enhanced reducibility of monoclinic ZrO<sub>2</sub> in the presence of rhodium species. A monoclinic ZrO<sub>2</sub> ( $\bar{1}11$ ) surface differs from a tetragonal ZrO<sub>2</sub>(101) surface: It presents a more diverse surface structure, where the coordination of oxygen anions to zirconium cations varies, whereas the oxygens considered on a tetragonal (101) surface are identical.<sup>23</sup> Our analysis covers all of the oxygens present in the first stoichiometric layer. We demonstrate that the release of oxygen from the most abundant ZrO<sub>2</sub> ( $\bar{1}11$ ) surface improves even in the presence of a single rhodium adatom. Additionally, we incorporate Rh<sub>4</sub> and Rh<sub>13</sub> nanoclusters as well as an infinite Rh<sub>40</sub> nanorod onto the ZrO<sub>2</sub> ( $\bar{1}11$ ) surface to address the effect of the size of the rhodium species on the reducibility of ZrO<sub>2</sub> (Figure 1). Because modeling of nanometer-size supported particles is computationally demanding, the infinite Rh<sub>40</sub> nanorod was chosen to mimic the perimeter of an arbitrarily large nanoparticle exposing a  $\bar{1}11$ -facet toward the support.

## COMPUTATIONAL DETAILS

Spin-paired periodic density functional theory (DFT) calculations were carried out using the Perdew–Burke–Ernzerhof (PBE) functional,<sup>25,26</sup> implemented in the grid-based projector augmented wave (GPAW) formalism.<sup>27–29</sup> The core electrons

Received: January 30, 2018

Revised: March 9, 2018

Published: March 13, 2018

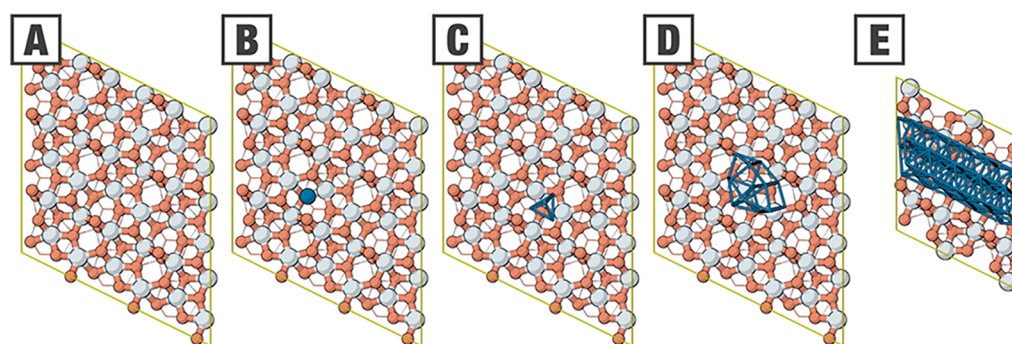


**Figure 1.** Employed models: (A)  $\text{ZrO}_2$ , (B)  $\text{Rh}_1/\text{ZrO}_2$ , (C)  $\text{Rh}_4/\text{ZrO}_2$ , (D)  $\text{Rh}_{13}/\text{ZrO}_2$ , and (E)  $\text{Rh}_{40}/\text{ZrO}_2$ . For visual clarity, polyatomic rhodium species are shown in wireframe. Color scheme: zirconium in light gray, oxygen in orange-red, and rhodium in teal.

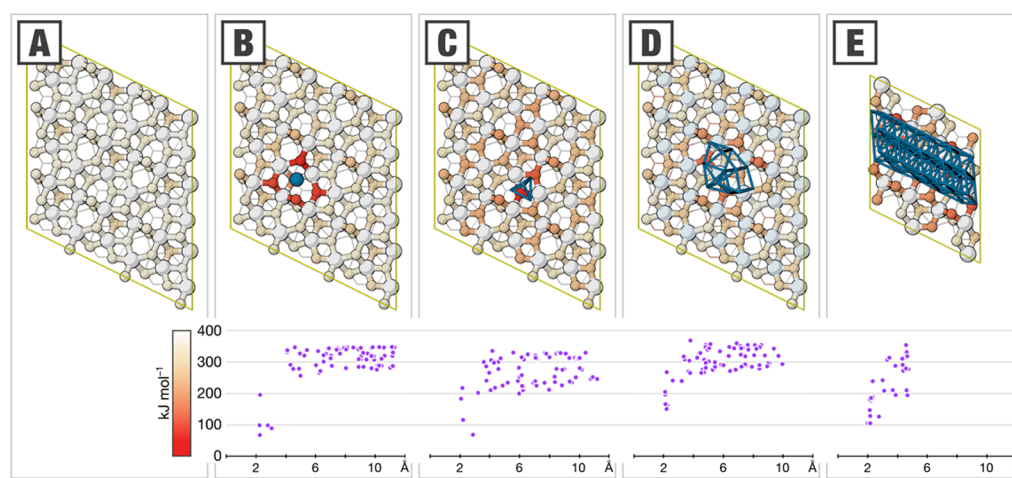


**Figure 2.** Reduction energy,  $\Delta E_{\text{R}}$ , mapped on the corresponding lattice oxygen atoms (structure figures) and as a function of the distance between the oxygen to be abstracted and the closest rhodium atom (plots): (A)  $\text{ZrO}_2$ , (B)  $\text{Rh}_1/\text{ZrO}_2$ , (C)  $\text{Rh}_4/\text{ZrO}_2$ , (D)  $\text{Rh}_{13}/\text{ZrO}_2$ , and (E)  $\text{Rh}_{40}/\text{ZrO}_2$ . For visual clarity, polyatomic rhodium species are shown in wireframe. For the identification of the kinds of atoms, the reader is kindly referred to Figure 1.

of heavy elements were represented with the PAW setups in the frozen-core approximation. The calculations included the following number of valence electrons: 15 for Rh, 12 for Zr, 6 for O, and 1 for H. Electron density was expanded on a uniform real-space grid with a maximum spacing of 200 mÅ. Each structure was allowed to relax with a threshold of 50 meV  $\text{\AA}^{-1}$  for the maximum residual force.

The  $\text{ZrO}_2$  ( $\bar{1}11$ ) surface was represented as a 2D slab constructed from the previously optimized bulk: the  $P2_1/c$  space group,  $a = 5.161 \text{ \AA}$ ,  $b = 5.231 \text{ \AA}$ ,  $c = 5.340 \text{ \AA}$  and  $\beta = 99.6^\circ$ . The lateral dimensions and the slab were varied depending on the size of the incorporated metal species to avoid interaction between the periodic images. The surface slabs for the pristine surface and the surface containing  $\text{Rh}_1$ ,  $\text{Rh}_4$ , and  $\text{Rh}_{13}$  species were  $(3 \times 3)$  repeated cells of two stoichiometric layers thick, that is, 72  $\text{ZrO}_2$  units. Surface slab that accommodated the  $\text{Rh}_{40}$  nanorod was a  $(2 \times 2)$  repeated cell of two stoichiometric layers thick, that is, 32  $\text{ZrO}_2$  units. The positions of the atoms in the bottom half of the slabs were fixed to their bulk positions.

Computational cells included enough vacuum along the nonperiodic direction to ensure the complete decay of the electron density at the edges. The reciprocal space was sampled with the  $\Gamma$ -point alone in the cases of the  $(3 \times 3)$  repeated cells and by a  $(2 \times 2)$  Monkhorst–Pack mesh of  $k$ -points in the

cases of the  $(2 \times 2)$  repeated cells. The computational approach has been validated in our previous papers.<sup>30,31</sup>

The reducibility of the considered systems was evaluated in terms of reduction energy,  $\Delta E_{\text{R}}$ , with respect to the gas-phase water molecule as  $\Delta E_{\text{R}} = E_{\text{red}} + (E_{\text{H}_2\text{O}} - E_{\text{H}_2}) - E_{\text{stoich}}$ , where  $E_{\text{red}}$  and  $E_{\text{stoich}}$  are the respective electronic energies of reduced and stoichiometric systems and  $E_{\text{H}_2}$  and  $E_{\text{H}_2\text{O}}$  correspond to the electronic energies of the gas-phase hydrogen and water molecules. We note that the choice of the gas-phase reference strongly affects the reduction energy. Using hydrogen and water as a reference helps us to avoid the known errors coming from DFT calculations of gas-phase oxygen.<sup>32,33</sup> The absolute values of the reduction energies change when the GGA+U level of theory is applied; however, we are mostly interested in trends and relative energy changes that are less sensitive to the chosen functional.

## RESULTS AND DISCUSSION

Figure 2 shows the reduction energy, respectively, mapped onto the corresponding anions and as a function of the distance between the lattice oxygen and the closest rhodium atom. It is clearly seen that the reduction energy of  $\text{ZrO}_2$  ( $\bar{1}11$ ) varies slightly from one anion to the other (Figure 2A), highlighting the differences in oxygen coordination. On average, the computed reduction energy is  $345 \pm 26 \text{ kJ mol}^{-1}$  and indicates

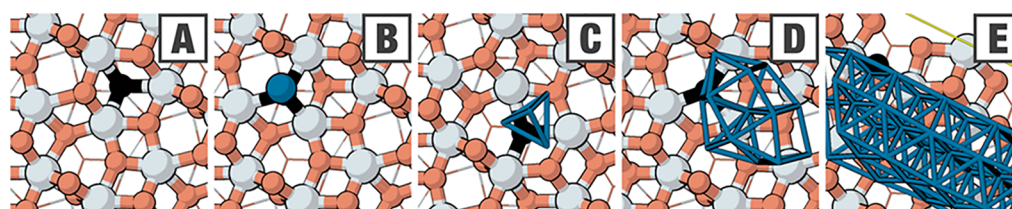


**Figure 3.** Structure of the most stable reduced systems: (A)  $\text{ZrO}_2$ , (B)  $\text{Rh}_1/\text{ZrO}_2$ , (C)  $\text{Rh}_4/\text{ZrO}_2$ , (D)  $\text{Rh}_{13}/\text{ZrO}_2$ , and (E)  $\text{Rh}_{40}/\text{ZrO}_2$ . For visual clarity, polyatomic rhodium species are shown in wireframe. Color scheme: zirconium in light gray, oxygen in orange-red, rhodium in teal, and oxygen vacancy in black.

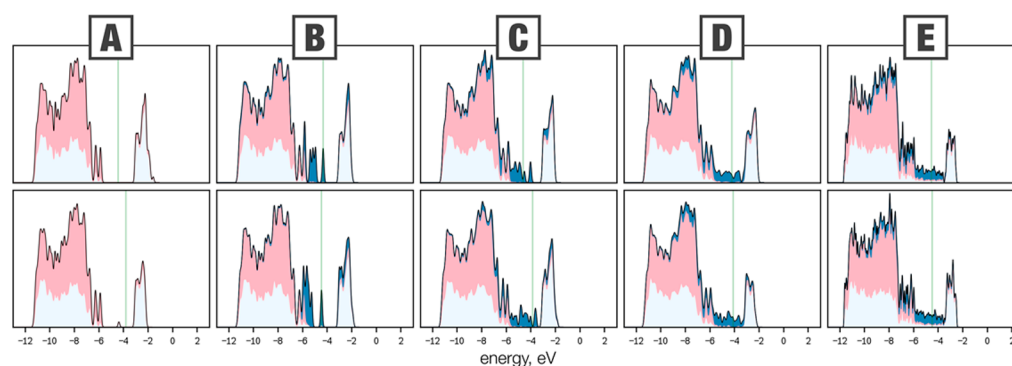


**Figure 4.** Density of states projected onto the orbitals of the corresponding atoms (in different colors) in stoichiometric (top row) and reduced (bottom row) systems: (A)  $\text{ZrO}_2$ , (B)  $\text{Rh}_1/\text{ZrO}_2$ , (C)  $\text{Rh}_4/\text{ZrO}_2$ , (D)  $\text{Rh}_{13}/\text{ZrO}_2$ , and (E)  $\text{Rh}_{40}/\text{ZrO}_2$ . For visual clarity, the values of the density of states are scaled by  $1/9$  for the Zr and O atoms and by  $1/n$  for the rhodium atoms in the cases of the  $\text{Rh}_n/\text{ZrO}_2$  systems. Coloring of electronic states: zirconium in light gray, oxygen in pink, and rhodium in teal. Vertical green lines indicate the position of the Fermi level.

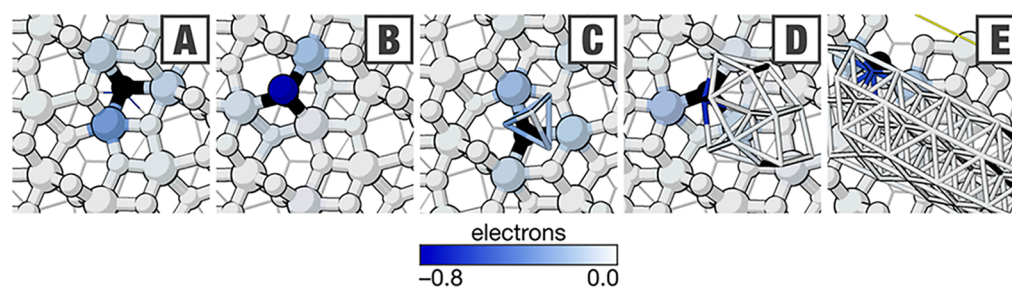


**Figure 5.** Change in the local Bader charges upon the formation of the most stable oxygen vacancy (in black): (A)  $\text{ZrO}_2$ , (B)  $\text{Rh}_1/\text{ZrO}_2$ , (C)  $\text{Rh}_4/\text{ZrO}_2$ , (D)  $\text{Rh}_{13}/\text{ZrO}_2$ , and (E)  $\text{Rh}_{40}/\text{ZrO}_2$ . For visual clarity, polyatomic rhodium species are shown in wireframe. For the identification of the kinds of atoms, the reader is kindly referred to Figure 3.

poor reducibility of the surface in line with the commonly accepted classification of zirconia being an irreducible oxide.<sup>34</sup>

Our calculations show that metallic rhodium strongly influences the reducibility, and the impact correlates with the distance between the oxygen to be abstracted and the closest rhodium atom (Figure 2B–E). We have divided the lattice positions into two groups: the distance is (1)  $<4$  Å and (2)  $>4$  Å. In the first group, the reduction energy is lowered substantially and is at best as low as ca.  $68 \text{ kJ mol}^{-1}$  in the presence of a single Rh adatom. For  $\text{Rh}_4/\text{ZrO}_2$ , the decrease is  $>80\%$  compared with bare  $\text{ZrO}_2(\bar{1}11)$ , being as small as for the single Rh atom. While for the larger rhodium species the effect is less pronounced, the reduction energies are still considerably lowered being ca.  $150 \text{ kJ mol}^{-1}$  ( $>55\%$ ) and ca.  $105 \text{ kJ mol}^{-1}$  ( $>69\%$ ) for the  $\text{Rh}_{13}/\text{ZrO}_2$  and  $\text{Rh}_{40}/\text{ZrO}_2$  systems, respectively. Similar influence of metal species on the reducibility of irreducible oxides has been previously evaluated computationally for  $\text{Au}/\text{MgO}$ ,<sup>19</sup>  $\text{Au}_n$  ( $n \leq 10$ )/tetragonal- $\text{ZrO}_2$ ,<sup>20</sup> and  $\text{Ru}_{10}$ /tetragonal- $\text{ZrO}_2$ ;<sup>21</sup> however, the magnitude of the positive effect of metals was found to be  $<55\%$  and  $<43\%$  for Au- and

Ru-based zirconia systems, respectively. Whether the differences in magnitude of enhanced reducibility between monoclinic and tetragonal  $\text{ZrO}_2$  are due to different metal species or the different polymorph of zirconia remains to be identified.

Figure 3 shows the structures for the studied systems with the best reducibility. Upon removal of a lattice oxygen, the metal part undergoes only minor changes in its geometry. As the most mobile species, the single rhodium adatom sometimes migrates to another surface site closer to the formed oxygen vacancy. We note that for  $\text{Rh}_{40}/\text{ZrO}_2$  the most reactive lattice oxygen is located behind the rod. However, if we focus on the front of the rod, which mimics the  $\text{Rh}(111)/\text{ZrO}_2$  interface for large Rh nanoparticles, the reduction energy for the most reactive oxygen is  $145 \text{ kJ/mol}$ , close to the value found for the  $\text{Rh}_{13}$  cluster.

The second group of the lattice positions, that is, the anions that are further than  $4$  Å away from the closest Rh atom, is characterized by significantly smaller changes in the reduction energies, as seen from the plots in Figure 2B–E. On average,

the reduction energy for these positions in the Rh/ZrO<sub>2</sub> systems is lowered by ca. <27% compared with the pristine ZrO<sub>2</sub> (111) surface. These findings suggest that there is a kind of “enhanced reduction zone” within ca. 4 Å from the Rh species.

To gain further understanding of enhanced reducibility, we analyzed the density of states and the local charges of the stoichiometric and reduced systems. In the case of the reduced systems, we considered only the structures with the lowest reduction energies, shown in Figure 3. As seen from Figure 4A, the band gap between the O 2p valence band and the Zr 4d conduction band state is >2 eV in the case of ZrO<sub>2</sub>(111). This indicates that the excess electrons left into the vacancy after the removal of lattice anions require a significant amount of energy to localize on the zirconium atoms. Oxygen removal from the lattice leaves two electrons into the vacancy and introduces vacancy-induced states into the middle of the gap. These cations altogether gain ca. 1.11 electrons, which is nearly what an anion in the stoichiometric surface has, according to the Bader analysis (Figure 5A).

The presence of on-surface Rh introduces changes to the electronic structure as the electronic states of Rh are in part hybridized with the valence band (Figure 4B–E). This leads to the narrowing of the band gap between the occupied oxygen states and the unoccupied rhodium states, effectively facilitating localization of the electrons left after the oxygen removal. The Bader analysis reveals that the adatom accepts ca. 0.90 electrons, while ca. 0.34 electrons are localized on three zirconium atoms located next to the oxygen vacancy (Figure 5B). The larger Rh species, that is, the Rh<sub>4</sub> and Rh<sub>13</sub> clusters and the Rh<sub>40</sub> nanorod, accommodate ca. 0.77 to 0.79 electrons. The remaining ca. 0.35 to 0.44 electrons are localized on the support. The three bottommost atoms in the Rh<sub>4</sub> cluster bear practically identical charges, while the top of the cluster is neutral (Figure 5C). In the cases of the Rh<sub>13</sub> cluster and the Rh<sub>40</sub> nanorod, the transferred electrons are majorly localized on a single Rh atom adjacent to the oxygen vacancy (Figure 5D,E). It is worth noting that we observe a qualitative trend between the reduction energy and the number of excess electrons accommodated by the Rh species: The more negative the charge on a Rh species, the lower the corresponding reduction energy.

## CONCLUSIONS

We reported DFT predictions of enhanced reducibility of monoclinic zirconia upon deposition of Rh species with varying size up to 40 Rh atoms. Our results demonstrate that the reduction energy with respect to the gas-phase water lowers by ca. 80% in the presence of a single Rh adatom or a Rh<sub>4</sub> nanocluster. With the increasing size of the Rh species, that is, in the presence of a Rh<sub>13</sub> nanocluster and a Rh<sub>40</sub> nanorod, the impact on the reducibility weakens but is still substantial. The positive effect of Rh owes to its ability to accommodate the excess electrons left after oxygen removal, supported by the analysis of the electronic structure. Overall, our findings suggest that the “redox” pathway of the WGS reaction might be possible over Rh/ZrO<sub>2</sub> systems due to metal-assisted oxygen removal from irreducible oxide. The effect of considerable increase in the oxide reducibility might take place for other metal/oxide systems that include commonly used irreducible oxides and other industrial processes that involve oxidation. Thus special care should be taken when interpreting

experimental and computational findings for oxidation processes over irreducible oxides.

## AUTHOR INFORMATION

### Corresponding Author

\*E-mail: karoliina.honkala@jyu.fi.

### ORCID

Karoliina Honkala: 0000-0002-3166-1077

### Notes

The authors declare no competing financial interest.

## ACKNOWLEDGMENTS

The work was funded by the Academy of Finland (<http://www.aka.fi/en/>, grant 277222). The electronic structure calculations were made possible by the computational resources provided by the CSC-IT Center for Science, Espoo, Finland (<https://www.csc.fi/en/>). We thank Prof. Leon Lefferts and Dr. Yingnan Zhao for fruitful discussions.

## REFERENCES

- (1) Gawande, M. B.; Pandey, R. K.; Jayaram, R. V. Role of Mixed Metal Oxides in Catalysis Science—versatile Applications in Organic Synthesis. *Catal. Sci. Technol.* **2012**, *2*, 1113.
- (2) Lee, D. W.; Yoo, B. R. Advanced Metal Oxide (Supported) Catalysts: Synthesis and Applications. *J. Ind. Eng. Chem.* **2014**, *20*, 3947–3959.
- (3) Védrine, J. Heterogeneous Catalysis on Metal Oxides. *Catalysts* **2017**, *7*, 341.
- (4) Zhang, J.; Zhong, Z.; Cao, X.-M.; Hu, P.; Sullivan, M. B.; Chen, L. Ethanol Steam Reforming on Rh Catalysts: Theoretical and Experimental Understanding. *ACS Catal.* **2014**, *4*, 448–456.
- (5) Bukur, D. B.; Todic, B.; Elbashir, N. Role of Water-Gas-Shift Reaction in Fischer–Tropsch Synthesis on Iron Catalysts: A Review. *Catal. Today* **2016**, *275*, 66–75.
- (6) Kalamaras, C. M.; Dionysiou, D. D.; Efstathiou, A. M. Mechanistic Studies of the Water-Gas Shift Reaction over Pt/Ce<sub>x</sub>Zr<sub>1-x</sub>O<sub>2</sub> Catalysts: The Effect of Pt Particle Size and Zr Dopant. *ACS Catal.* **2012**, *2*, 2729–2742.
- (7) Kalamaras, C. M.; Americanou, S.; Efstathiou, A. M. “Redox” vs “associative Formate with -OH Group regeneration” WGS Reaction Mechanism on Pt/CeO<sub>2</sub>: Effect of Platinum Particle Size. *J. Catal.* **2011**, *279*, 287–300.
- (8) Tibiletti, D.; Meunier, F. C.; Goguet, A.; Reid, D.; Burch, R.; Boaro, M.; Vicario, M.; Trovarelli, A. An Investigation of Possible Mechanisms for the Water-Gas Shift Reaction over a ZrO<sub>2</sub>-Supported Pt Catalyst. *J. Catal.* **2006**, *244*, 183–191.
- (9) Azzam, K.; Babich, I.; Seshan, K.; Lefferts, L. Bifunctional Catalysts for Single-Stage Water–gas Shift Reaction in Fuel Cell applications. Part 1. Effect of the Support on the Reaction Sequence. *J. Catal.* **2007**, *251*, 153–162.
- (10) Jacobs, G. Water-Gas Shift: Comparative Screening of Metal Promoters for Metal/ceria Systems and Role of the Metal. *Appl. Catal., A* **2004**, *258*, 203–214.
- (11) Yao, H. Ceria in Automotive Exhaust Catalysts I. Oxygen Storage. *J. Catal.* **1984**, *86*, 254–265.
- (12) Ruiz Puigdollers, A.; Illas, F.; Pacchioni, G. ZrO<sub>2</sub> Nanoparticles: A Density Functional Theory Study of Structure, Properties and Reactivity. *Rend. Lincei* **2017**, *28*, 19–27.
- (13) Chen, H.-L.; Chang, J.-G.; Chen, H.-T. Origin of Doping Effects on the Oxygen Storage Capacity of Ce<sub>1-x</sub>M<sub>x</sub>O<sub>2</sub> (M = Fe, Ru, Os, Sm, Pu). *Chem. Phys. Lett.* **2011**, *502*, 169–172.
- (14) Chen, H.-T. First-Principles Study of CO Adsorption and Oxidation on Ru-Doped CeO<sub>2</sub> (111) Surface. *J. Phys. Chem. C* **2012**, *116*, 6239–6246.

- (15) Querino, P. S.; Bispo, J. R. C.; Rangel, M. do C. The Effect of Cerium on the Properties of Pt/ZrO<sub>2</sub> Catalysts in the WGSR. *Catal. Today* **2005**, *107–108*, 920–925.
- (16) Otroshchenko, T. P.; Kondratenko, V. A.; Rodemerck, U.; Linke, D.; Kondratenko, E. V. Non-Oxidative Dehydrogenation of Propane, N-Butane, and Isobutane over Bulk ZrO<sub>2</sub>-Based Catalysts: Effect of Dopant on the Active Site and Pathways of Product Formation. *Catal. Sci. Technol.* **2017**, *7*, 4499–4510.
- (17) Otroshchenko, T.; Kondratenko, V. A.; Rodemerck, U.; Linke, D.; Kondratenko, E. V. ZrO<sub>2</sub>-Based Unconventional Catalysts for Non-Oxidative Propane Dehydrogenation: Factors Determining Catalytic Activity. *J. Catal.* **2017**, *348*, 282–290.
- (18) Otroshchenko, T.; Sokolov, S.; Stoyanova, M.; Kondratenko, V. A.; Rodemerck, U.; Linke, D.; Kondratenko, E. V. ZrO<sub>2</sub>-Based Alternatives to Conventional Propane Dehydrogenation Catalysts: Active Sites, Design, and Performance. *Angew. Chem., Int. Ed.* **2015**, *54*, 15880–15883.
- (19) Graf, P. O.; de Vlieger, D. M.; Mojet, B. L.; Lefferts, L. New insights in reactivity of hydroxyl groups in water gas shift reaction on Pt/ZrO<sub>2</sub>. *J. Catal.* **2009**, *262*, 181–187.
- (20) Franchini, C. A.; Duarte de Farias, A. M.; Albuquerque, E. M.; dos Santos, R.; Fraga, M. A. Single-State Medium Temperature Water-Gas-Shift Reaction over Pt/ZrO<sub>2</sub>-Support Structural Polymorphism and Catalyst Deactivation. *Appl. Catal., B* **2012**, *117–118*, 302–209.
- (21) Chenu, E.; Jacobs, G.; Crawford, A. C.; Keogh, R. A.; Patterson, P. M.; Sparks, D. E.; Davis, B. H. Water-Gas-Shift: an examination of Pt promoted MgO and tetragonal and monoclinic ZrO<sub>2</sub> by in situ drifts. *Appl. Catal., B* **2005**, *59*, 45–56.
- (22) Honkala, K.; Häkkinen, H. Au Adsorption on Regular and Defected Thin MgO(100) Films Supported by Mo. *J. Phys. Chem. C* **2007**, *111*, 4319–4327.
- (23) Puigdollers, A. R.; Pacchioni, G. CO Oxidation on Au Nanoparticles Supported on ZrO<sub>2</sub>: Role of Metal/Oxide Interface and Oxide Reducibility. *ChemCatChem* **2017**, *9*, 1119–1127.
- (24) Puigdollers, A. R.; Schlexer, P.; Tosoni, S.; Pacchioni, G. Increasing Oxides Reducibility: The Role of Metal/oxide Interfaces in the Formation of Oxygen Vacancies. *ACS Catal.* **2017**, *7*, 6493–6513.
- (25) Perdew, J. P.; Burke, K.; Ernzerhof, M. Generalized Gradient Approximation Made Simple. *Phys. Rev. Lett.* **1996**, *77*, 3865–3868.
- (26) Perdew, J. P.; Burke, K.; Ernzerhof, M. Generalized Gradient Approximation Made Simple—Errata. *Phys. Rev. Lett.* **1997**, *78*, 1396.
- (27) Enkovaara, J.; Rostgaard, C.; Mortensen, J. J.; Chen, J.; Dulak, M.; Ferrighi, L.; Gavnholt, J.; Glinsvad, C.; Haikola, V.; Hansen, H. A.; et al. Electronic Structure Calculations with GPAW: A Real-Space Implementation of the Projector Augmented-Wave Method. *J. Phys.: Condens. Matter* **2010**, *22*, 253202.
- (28) Mortensen, J. J.; Hansen, L. B.; Jacobsen, K. W. Real-Space Grid Implementation of the Projector Augmented Wave Method. *Phys. Rev. B: Condens. Matter Mater. Phys.* **2005**, *71*, 1–11.
- (29) Larsen, A. H.; Mortensen, J. J.; Blomqvist, J.; Castelli, I. E.; Christensen, R.; Dulak, M.; Friis, J.; Groves, M. N.; Hammer, B.; Hargus, C.; et al. The Atomic Simulation Environment—A Python Library for Working with Atoms. *J. Phys.: Condens. Matter* **2017**, *29*, 273002.
- (30) Bazhenov, A. S.; Honkala, K. Understanding Structure and Stability of Monoclinic Zirconia Surfaces from First-Principles Calculations. *Top. Catal.* **2017**, *60* (6–7), 382–391.
- (31) Bazhenov, A. S.; Lefferts, L.; Honkala, K. Adsorption and Activation of Water on Cuboctahedral Rhodium and Platinum Nanoparticles. *J. Phys. Chem. C* **2017**, *121*, 4324–4331.
- (32) Hammer, B.; Hansen, L. B.; Nørskov, J. K. Improved Adsorption Energetics within Density Functional Theory using revised perdew-Burke-Ernzerhof Functionals. *Phys. Rev. B: Condens. Matter Mater. Phys.* **1999**, *59*, 7413–7421.
- (33) Klüpfel, S.; Klüpfel, P.; Jónsson, H. The Effect of the Perdew-Zunger Self-Interaction Correction to Density functionals on the Energetics of Small Molecules. *J. Chem. Phys.* **2012**, *137*, 124102.
- (34) Syzgantseva, O. A.; Calatayud, M.; Minot, C. Revealing the Surface Reactivity of Zirconia by Periodic DFT Calculations. *J. Phys. Chem. C* **2012**, *116*, 6636–6644.